Effect of the Niobium Doping Concentration on the Charge Storage Mechanism of Mesoporous Anatase Beads as an Anode for High-Rate

N.B. When citing this work, cite the original published paper.

(article starts on next page)

ACS **APPLIED**
ENERGY MATERIALS

Article

Effect of the Niobium Doping Concentration on the Charge Storage Mechanism of Mesoporous Anatase Beads as an Anode for High-Rate Li-Ion Batteries

Carmen Cavallo,* Giulio Calcagno, Rodrigo Pereira de Carvalho, Matthew Sadd, Bruno Gonano, C. Moyses Araujo, Anders E.C. Palmqvist, and Aleksandar Matic*

Cite This: *ACS Appl. Energy Mater.* 2021, 4, 215–225

Read Online

ACCESS | 📊 Metrics & More | 📄 Article Recommendations | 🆂🅸 Supporting Information

ABSTRACT: A promising strategy to improve the rate performance of Li-ion batteries is to enhance and facilitate the insertion of Li ions into nanostructured oxides like TiO_2. In this work, we present a systematic study of pentavalent-doped anatase TiO_2 materials for third-generation high-rate Li-ion batteries. Mesoporous niobium-doped anatase beads (Nb-doped TiO_2) with different Nb^{5+} doping (*n*-type) concentrations (0.1, 1.0, and 10% at.) were synthesized via an improved template approach followed by hydrothermal treatment. The formation of intrinsic *n*-type defects and oxygen vacancies under RT conditions gives rise to a metallic-type conduction due to a shift of the Fermi energy level. The increase in the metallic character, confirmed by electrochemical impedance spectroscopy, enhances the performance of the anatase bead electrodes in terms of rate capability and provides higher capacities both at low and fast charging rates. The experimental data were supported by density functional theory (DFT) calculations showing how a different *n*-type doping can be correlated to the same electrochemical effect on the final device. The Nb-doped TiO_2 electrode materials exhibit an improved cycling stability at all the doping concentrations by overcoming the capacity fade shown in the case of pure TiO_2 beads. The 0.1% Nb-doped TiO_2-based electrodes exhibit the highest reversible capacities of 180 mAh g^{-1} at 1C (330 mA g^{-1}) after 500 cycles and 110 mAh g^{-1} at 10C (3300 mA g^{-1}) after 1000 cycles. Our experimental and computational results highlight the possibility of using *n*-type doped TiO_2 materials as anodes in high-rate Li-ion batteries.

KEYWORDS: high-rate batteries, Li-ion batteries, mesoporous niobium doped anatase, n-type doped anode materials, DFT calculation, Rietveld refinement
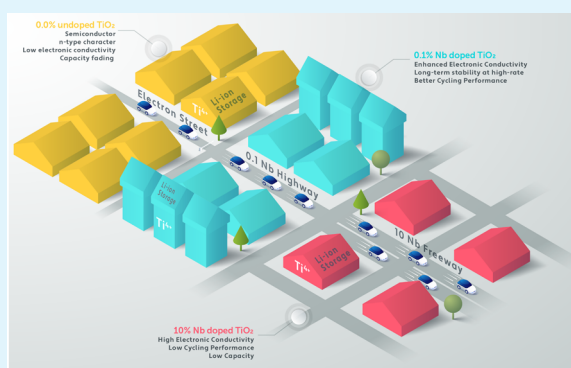
■ INTRODUCTION

As the field of use of battery systems further expands, batteries with higher capacity, cyclability, and safety are deemed necessary. Non-aqueous rechargeable Li-ion batteries are among the most prominent energy storage devices, and their development represents a prodigious success of modern materials chemistry. Graphite is today's commercially established anode material, but with not just a few limitations.[1] Low operational voltage (0.1 V *vs* Li/Li$^+$), connected with the risk of lithium plating during overcharge, and severe structural collapse are some of the most common problems that need to be mitigated.[2] Moreover, the applicability of graphite anode materials is particularly restricted to low rate applications.[3−6]

Several requirements should be addressed to find suitable high-rate anodes. A low volume change during the Li-ion insertion/desertion is necessary for good cycling stability. Short diffusion paths for fast lithium insertion/desertion, a low intercalation potential for lithium, and cheap and environ-

mentally benign raw materials are also highly desired attributes. Additionally, nanomaterials with a large exposed surface area have shown to allow for more accessible lithium insertion channels and improved device performance.[7]

TiO_2-based nanomaterials and, in particular, the polymorphs anatase and TiO_2(B) are promising as negative electrodes due to their high structural stability, thanks to the low volume change during cycling (∼4%).[1] Unfortunately, the poor electronic conductivity and the low ionic diffusivity, which influence the Li insertion/desertion in TiO_2, are affecting their use in practice.[8]

Herein, we aim at overcoming the low electronic conductivity, the low ion diffusivity, and the capacity fading of anatase by introducing pentavalent niobium ion doping and directly using our microbeads as anodes for fast rechargeable Li-ion batteries. The 3D hierarchical porous structure of the microbeads needs to be combined with an increased electronic conductivity of the semiconducting TiO_2 without affecting the Ti^{4+} available reduction sites.[9,10] This can be achieved by introducing Nb^{5+} ions into the TiO_2 lattice through a donor-type doping process.[11−14] The ionic radius of Nb^{5+} is only 5.8% larger than that of Ti^{4+} (0.64 Å vs 0.605 Å), and Nb^{5+} can thus easily substitute Ti^{4+} in the lattice of TiO_2 in a wide range of concentrations. Moreover, the solvo-thermal synthesis process used in this work allows the insertion of Nb^{5+} into the anatase lattice without undesirable phase transitions, in contrast to previously reported preparation routes.[15]

Undoped anatase TiO_2 has a natural n-type character regulated by the following equilibrium, which leads to the natural formation of oxygen vacancies ($V_O^{\cdot\cdot}$):

$$TiO_2 \overset{RT}{\Rightarrow} TiO_{2-x} + V_o^{\cdot\cdot} + \frac{x}{2}O_2 + 2e^- \tag{1}$$
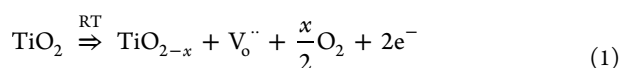
According to Körner and Elsässer,[16] Nb doping may lead to an increase in the n-type character of anatase TiO_2. To compensate the excessive charge of Nb^{5+} in substitution to Ti^{4+}, one Ti cation vacancy may be created per four Nb introduced or the stoichiometric reduction of Ti^{4+} to Ti^{3+} per Nb introduced may happen depending on the processing conditions, which introduces shallow donor levels below the CB edge of TiO_2 and increases the metallic character.[17] This particular behavior is only observed for the anatase phase of the different TiO_2 polymorphs. Indeed, Yang et al. calculated that Nb-doped anatase TiO_2 shows an n-type half-metallic character, while Nb-doped rutile TiO_2 shows an insulating character.[13,18] As reported by Yue et al., the incorporation of Nb^{5+} into the anatase TiO_2 lattice modifies the band structure of the anatase and the Li-ion (charge) storage mechanism is strongly dependent on the doping concentration.[19]

We report a detailed computational and experimental study of donor-type doped TiO_2 microbeads at different dopant concentrations (undoped (0.0%) and 0.1, 1.0, and 10% at. Nb-doped TiO_2). The contribution of the Nb^{5+} doping on the structural and electronic properties and the charge storage mechanism is well defined in terms of the physicochemical properties of the anatase phase and the atomic doping concentration.[20]

Moreover, fast rechargeability is receiving more and more attention as one of the main research objectives for Li-ion battery development.[21] The scientific community has focused a lot of effort in pushing the boundaries of rate capability for Li-ion cells and achieving the goal of extreme fast charging.[22]

Our results show that the synergistic effect of the mesoporous bead morphology and the Nb^{5+} doping (n-type) significantly improves the cycling life by reducing the capacity fading and increasing the specific nominal capacity both at low (1C) and at high (from 10C up to 100C) current rates, suggesting the use of these materials for both low and high rate capability fast rechargeable Li-ion batteries.

■ RESULTS AND DISCUSSION

The as-synthesized samples show a color change from white (0.1% Nb doping) to yellow (10% Nb doping) due to the increase in the niobium amount inside the structure,[23] as visible in Figure S1.

The X-ray diffraction (XRD) patterns, reported in Figure 1a, confirm that all the samples are monophasic with reflections
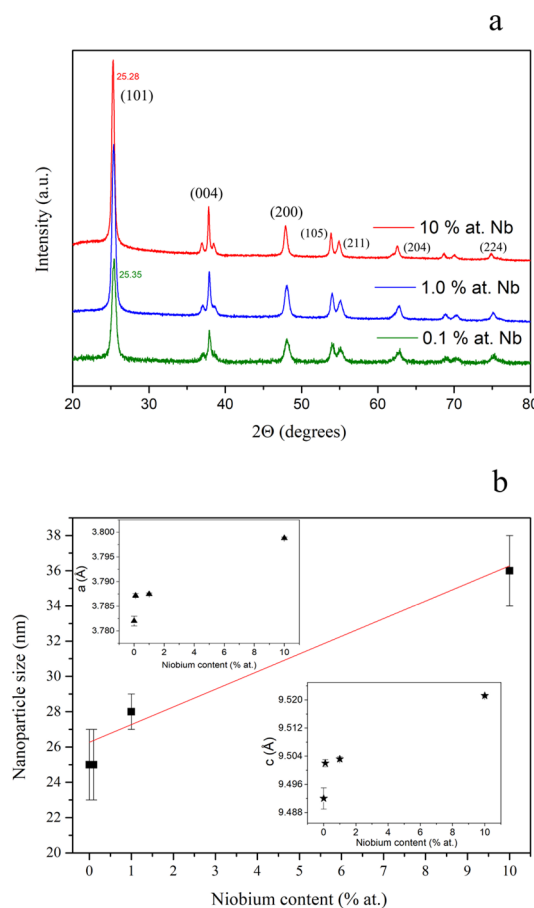
Figure 1. (a) X-ray diffractograms of TiO_2 materials Nb-doped at 0.1, 1.0, and 10% at. Nb. The (101) peak shifted from 25.35° 2θ at 0.1% at. to 25.28° at 10% at. Nb. (b) Nanoparticle size determined from the Rietveld analysis and, in the top and bottom insets, the unit cell parameters size (a and c, respectively) as a function of Nb content.

ascribed only to the anatase TiO_2 phase.[24] The employed temperature-controlled sol−gel synthesis method allows the formation of phase-pure (tetragonal, $I41/amd$) doped anatase microbeads, reaching the goal of avoiding traces of other TiO_2 phases.[18,25] The diffraction pattern related to the pure sample (0.0% Nb) is reported in Figure S2. The diffraction peaks related to the (101) planes of anatase TiO_2 gradually shift to lower 2θ values with Nb doping due to the enlargement of the unit cell caused by the substitution of Ti^{4+} by Nb^{5+}.[26] The $\Delta\theta$ shift between the most intense peak (101) of 0.1% vs 10% is 0.07° and can be translated to a lattice expansion of about 0.012%,[27] which points to the formation of a substitutional solid solution. Considering the similarity in ionic radii and previous results reported in literature,[18] it is reasonable to assume that Nb^{5+} occupies Ti^{4+} sites and that the lattice constants of a Nb-doped TiO_2 crystal will be larger than those of the pure TiO_2 crystal. In addition, the calculated XRD patterns in Figure S3 show good agreement with the experimental findings and the same relative shift is found there.

The results of the Rietveld analysis are reported in Figure 1b, show a dependency of the nanoparticle size vs the niobium

content, and confirm the presence of larger crystals in the doped sample. The nanoparticle size increases linearly with niobium doping.

As expected, the doping leads to an increase in the a and c axes of the anatase crystal lattice (see insets in Figure 1b). Therefore, the overall volume of the unit cell will increase based on the following equation:

$$V = a^2 \times c \tag{2}$$

The volume expansion confirms the hypothesis that the Nb^{5+} ions are incorporated into the anatase lattice by substitution of Ti^{4+}. In addition, the slightly broadened peaks found for the 0.1% sample become sharper due to the increase in the particle size at higher doping.

In Figure 2, scanning electron microscopy images with low (top panel) and high (bottom panel) magnification of 0.1%
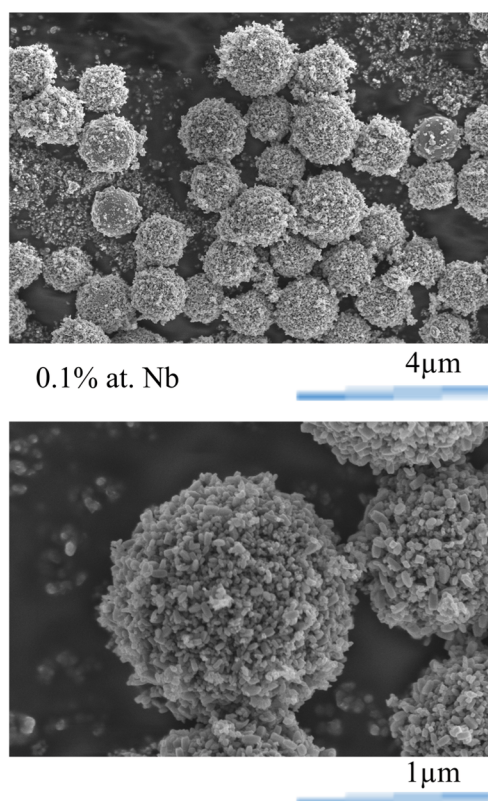
Figure 2. Scanning electron microscopy images of Nb-doped TiO_2 at 0.1% at.. The higher magnification reveals the well-defined 3D hierarchical structure of the beads.

Nb-doped TiO_2 are reported to illustrate the morphology of the as-synthesized materials. All the materials exhibit microspherical morphology as a result of the template-assisted (HDA) sol−gel synthesis. SEM images of the pure, 1.0%, and 10% are reported in Figures S4−S6, respectively. The EDX spectra related to the SEM images are reported in Figure S7. The ratio between titanium and niobium is in agreement with the synthesis parameter. The beads are well defined as nanoparticle agglomerates with a 3D hierarchical morphology of about one and a half micrometers in size.

The morphologies at micro- and nanoscopic levels for 0.1 and 10% at. Nb-doped TiO_2 are shown in Figure 3. HRTEM images recorded at low magnification (×20k) (Figure 3a,d) show a spherical organization of the nanoparticles in order to
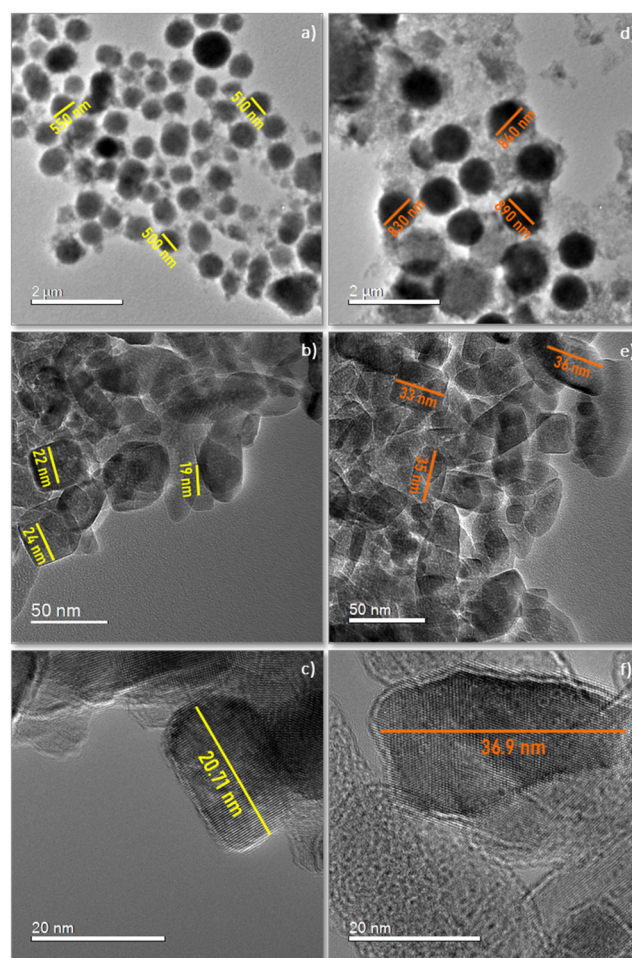
Figure 3. High-resolution transmission electron microscopy (HRTEM) images recorded at various magnifications (×20k, ×140k, and ×600k) for two compositions: (a−c) 0.1% at. Nb at 2 μm, 50 nm, and 20 m, respectively, and (d−f) 10% at. Nb reported in comparison at the same magnifications. Sizes of the beads and nanoparticles are evidenced by yellow and orange lines for 0.1 and 10% at. Nb, respectively.

minimize the surface energy for both compositions. A variation of the diameter of the spheres is evidenced, depending also on the composition. Figure 3a indicates an average diameter of 500 μm for the lowest doping level (0.1% at. Nb) compared to a larger diameter, 850 μm, for 10% at. Nb (Figure 3d). HRTEM images at medium magnifications reveal a distribution of randomly oriented rice-grain- or cube-shaped nanoparticles. Statistical analysis of Figure 3b shows an average particle size close to 23 nm, while larger (≈35 nm) nanoparticles are consistently observed for the 10% at. doped TiO_2 (Figure 3e). Two images (Figure 3c,f) acquired at high magnification (×600k) illustrate this result. It has to be noted here that these observations are in good agreement with the values extracted from the Rietveld refinements (25 nm vs 35 nm) of X-ray diffraction data.

N2 adsorption/desorption measurements were performed to investigate the mesoporosity of the materials. All the isotherms belonged to type IV adsorption isotherm according to IUPAC classification and exhibited an H2 hysteresis loop at higher relative pressure, which confirmed the characteristics of mesopores, as shown in Figure S8. The pore size distribution, reported in Figure 4a, is independent of the doping

a

b

399 cm^{-1}
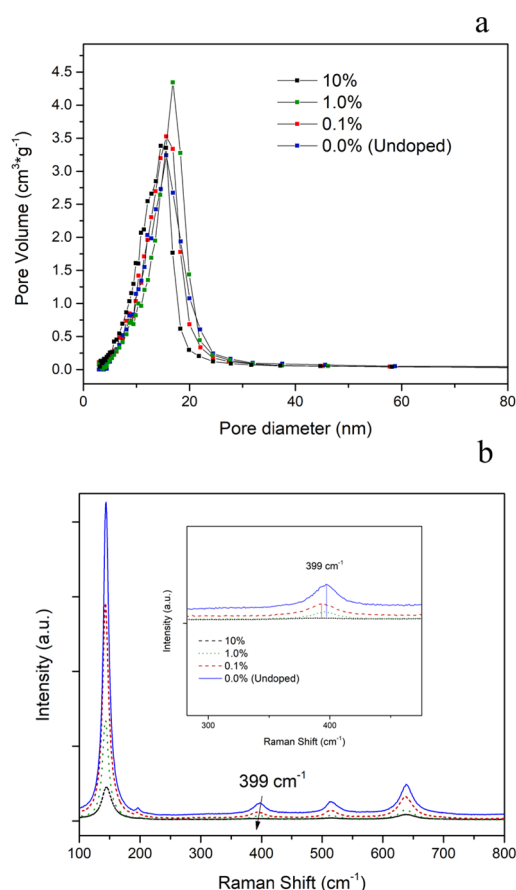
Figure 4. (a) Pore size distributions and (b) Raman spectra of the Nb-doped TiO_2 materials.

concentration and falls in the mesoporous range, with the peaks centered between 15 and 17 nm. The BET surface area is relatively high, 70−100 m^2 g^{-1}. It increases with increasing Nb-doping concentration up to 1%, as shown in Table 1, but is reduced at the highest Nb concentration, which is consistent with the trend of the increase in the grain size.

Table 1. Specific Surface Area Values of the Nb-Doped TiO_2 Materials

sample	specific surface area (m^2 g^{-1})
undoped (0.0%)	84.4 ± 0.3
0.1%	92.1 ± 0.3
1.0%	100.4 ± 0.3
10%	70.3 ± 0.3

Raman spectroscopy is an essential analysis method for the study of doped TiO_2 for its high sensitivity to the microstructure, and in this study, it is used to understand how the doping changes the physical properties of the anatase.

In Figure 4b, the Raman spectra of Nb-doped TiO_2 with different Nb contents all show the characteristic modes of anatase TiO_2.[19] No impurity phase is observed based on the absence of additional bands. Bands centered at 145, 399, 517, and 639 cm^{-1} are associated with Eg (n6), B1g, A1g, and Eg (n1) modes, respectively. The B1g (399 cm^{-1}) mode exhibits a slight shift to lower wavenumbers with increasing Nb concentration, as reported in the inset of Figure 4b. Since the B1g mode is related to the stretching of Ti−O bonds, the

observed shift is in line with Nb^{5+} being incorporated into the TiO_2 lattice, in good agreement with the XRD results. Moreover, the shift at a lower wavenumber further confirms the substitutional nature of the solid solution of Nb-doped anatase. However, the wavenumber only shifts to a lower value between the undoped sample and the 0.1% Nb-doped sample. This suggests that out of the four measured samples, the Ti−O bond reaches a maximum relaxation for the 0.1% Nb-doped sample and no further relaxation is observed in the 1.0% nor the 10% sample. This can be attributed to the increasing particle size of the samples with increased doping, shown in Figure 1b, and the confocal nature of the measurements.

DFT calculations were performed to better understand the effect on the electronic properties of Nb doping. The electronic density of states (DOS) projected for each atomic species and normalized by their respective number of atoms in the supercell is presented in Figure 5 for undoped (0.0%) anatase TiO_2 and 1.0% at. and 10% at. Nb-doped TiO_2. A closer look at the Fermi energy level (the zero-energy vertical line in the plot) shows the effect of Nb doping on the electronic structure. Starting with 1.0% Nb-doped TiO_2 (Figure 5 b), the Fermi energy level is shifted into the bottom of the conduction band, which in turn changes the compound toward a metallic-like character. The occupation of the conduction band states then increases for the 10% Nb-doped TiO_2 (Figure 5c) without changing the shape of the DOS, i.e., the topology (shape) of the band structure is unaffected upon the doping of the material. Nevertheless, filling the conduction band as a direct consequence of the n-type doping could have a negative impact on the lithiation process and the complementary reduction Ti^{4+} sites.

Indeed, upon lithiation, Ti^{4+} will be reduced to Ti^{3+}, accommodating the incoming electron. These Ti empty states are located at the conduction band and being filled by n-doping. Consequently, this is translated to less Ti states available for reduction. Accordingly, the conduction bands presented in Figure 5a−c have a significant contribution from Ti states even with Nb present. This effect is accentuated in the 10% sample, where the conduction band is even further populated. Moreover, this higher doping concentration also results in a greater contribution of Nb empty states for the conduction band, suggesting a possible redox activity of Nb ions. In addition, Figure 4d shows the average oxidation state (AOS) of Ti and Nb, as obtained by Bader charge analysis, and how it changes with doping concentration.

This AOS was taken as an oxidation state averaged by the respective atoms/species in the cell and shifted by the Ti average oxidation state in the undoped (0.0%) anatase TiO_2 (the dashed horizontal line in Figure 5d). Hereby, Nb has a higher AOS than Ti by approximately one unit, although both AOS tend to decrease for higher doping concentration. A first approximation of the lithiation/delithiation voltage could be obtained by using eq 3 (see the Experimental Section) and is presented in Figure 5e. For the undoped TiO_2, the obtained lithiation/delithiation voltage is 2.04 V (vs Li/Li$^+$). The Nb-doped materials show a decrease in the lithiation/delithiation voltage with increased doping concentration. Likewise, the voltage also shows dependence on the lithiation site with a significant drop when the lithiation happens in the Nb-rich sites. The Nb-rich/poor calculated structures are reported in Figure S9. We obtain 1.93 V (1.87 V) vs Li/Li$^+$ for Nb-poor (Nb-rich) sites and 1.45 V (1.23 V) vs Li/Li$^+$ for Nb-poor (Nb-rich) sites in the cases of 1.0% and 10% doping,
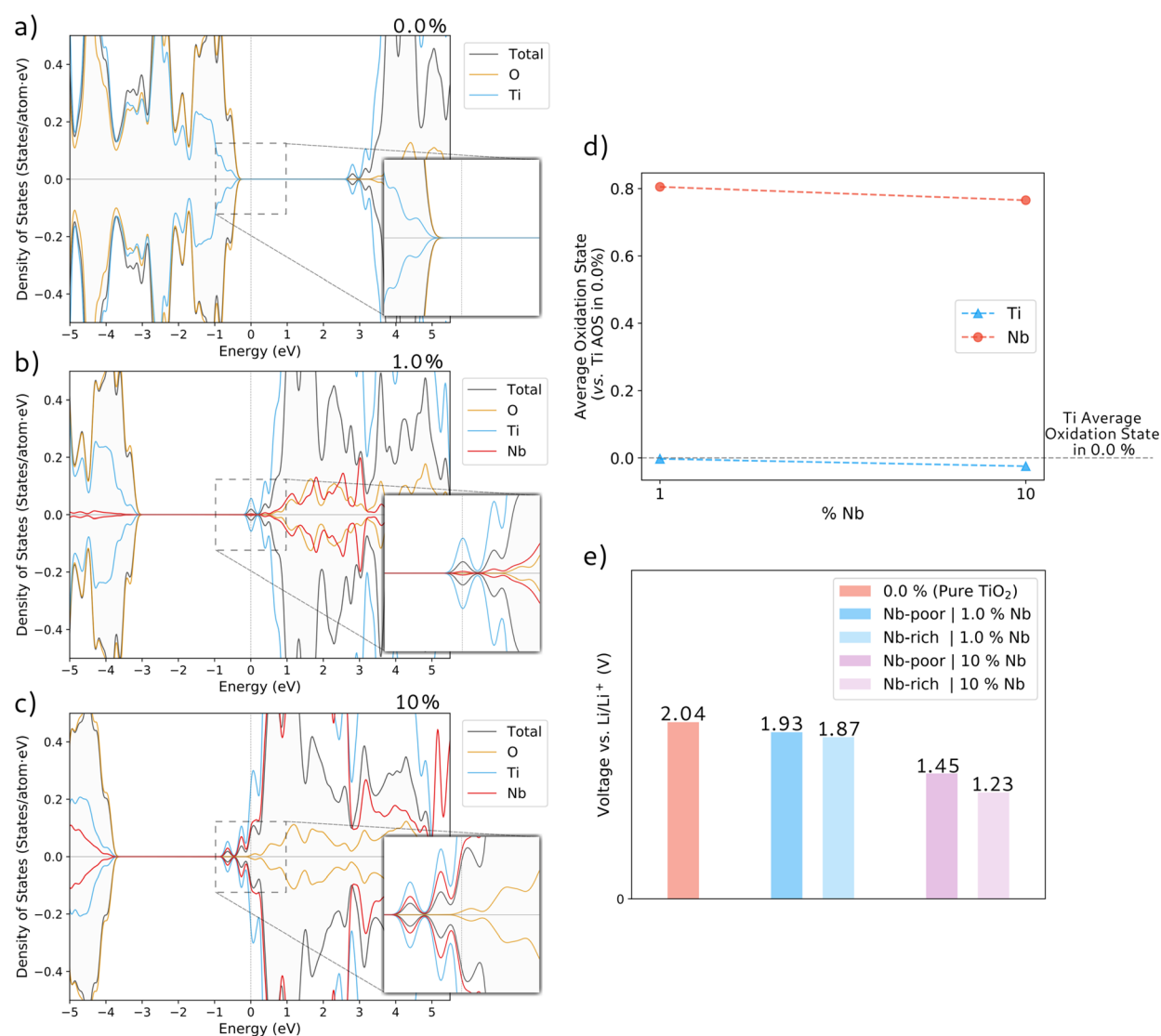
Figure 5. Electronic density of states projected for each atomic species and normalized by their respective number of atoms in the supercell for the (a) 0.0, (b) 1.0, and (c) 10% at. Nb-doped anatase TiO_2. The Fermi energy level is represented by the zero-energy vertical line. The Ti states are higher than the total states because of normalization, as we divide by their respective number of atoms in the unit cell. (d) Average oxidation state of each species as a function of doping level. The zero horizontal line is the average oxidation state of Ti calculated for the pure TiO_2. (e) Lithiation voltage (vs Li/Li$^+$) for the different doping concentration and for Nb-rich/poor environments, see text.

respectively. For the 10% doping, however, a clear definition of the Nb-poor region is limited by the size of the cell. Thus, the obtained voltages translate the effect of a smaller/bigger amount of Nb surrounding the Li$^+$ site for the respective case (poor/rich). Finally, the calculation suggests that the addition of small amounts of Nb could possibly improve the overall performance of the material by enhancing its metallic-like character while offering small effects on its electrochemical properties. In contrast, a higher concentration of Nb may lead to inferior electrochemical performance.

The Nb-doped anatase electrodes were electrochemically evaluated using a half-cell configuration vs lithium metal. The electrochemical impedance spectra and the fits to equivalent circuits are reported in Figure 6. At high frequencies, the intercept at Z′ corresponds to R_s and represents a combination of the electrolyte resistance, intrinsic resistance of substrate, and contact resistance at the composite electrode/current collector interface. The CPE$_{dl}$ (constant phase element) is associated to the double-layer capacitance of the active
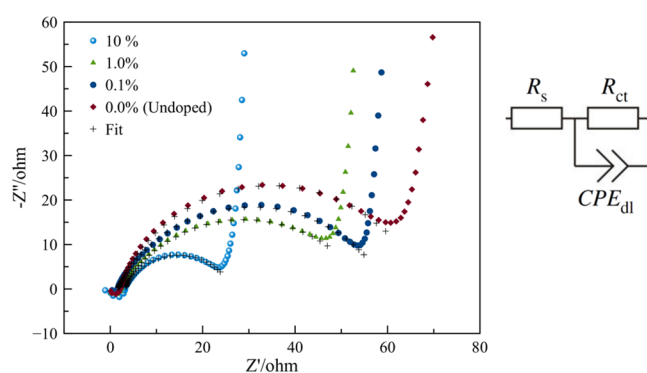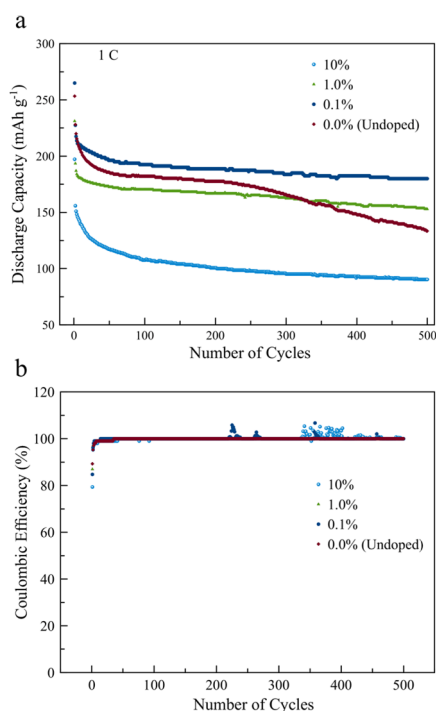

Figure 6. Electrochemical impedance spectra. Fit of the first semicircle and related equivalent circuit of the undoped and Nb-doped TiO_2 electrodes vs lithium metal.

material. All the electrodes show similar values for both parameters. The differences appear in the semicircle in the

high-frequency range, which corresponds to the charge-transfer resistance (R_{ct}) caused by the Faradaic reactions. As expected, the increase in doping amount is reflected in a decrease in the semicircle radius and the R_{ct} decreases from 66 Ω of the undoped material to 58, 53, and 23 Ω for 0.1%, 1.0%, and 10%, respectively. Therefore, the EIS data suggest an increase in conductivity, which could be connected to the shift of the Fermi level into the conduction band upon doping, as found by the DFT calculations.

The mesoporous anatase bead morphology is able to store charge through three mechanisms: faradaic redox reactions associated to the insertion/de-insertion of lithium ions; formation of a double layer, i.e., capacitance; and fast surface redox reactions giving rise to a pseudocapacitance. Specifically, the pseudocapacitance obtained by nanosizing a transition-metal oxide is defined as extrinsic insertion pseudocapacitance.[28] In a previous publication,[9] we showed that the pseudocapacitive contribution to the total charge were around ∼30%, determined by cyclic voltammetry at 0.5 mV s^{-1}. Smarsly et al. demonstrated that the increase in conductivity through doping is followed by an increase in the pseudocapacitive contributions.[19] We, therefore, expect an increase in pseudocapacitance for our Nb-doped TiO_2 electrodes, leading to higher specific capacities and improved rate performance. Figure 7a shows the specific discharge

The Coulombic efficiency increases to 98.7% after a few cycles and remains greater than 99.5% thereafter, as reported in Figure 7b. Galvanostatic charge/discharge curves at a 1C rate for all the samples are reported in Figure 8. Differential curves of the respective galvanostatic discharges are shown in Figure S10. As we reported in our previous works,[9,20] CV or differential curves demonstrated the lithium insertion mechanism and the high structural stability of the anodes. In a typical CV curve[9] performed at 0.1 mV s^{-1}, the main cathodic (∼1.7 V) and anodic (∼2.1 V) peaks correspond to lithium insertion and extraction, respectively. The process is characterized by a phase coexistence of tetragonal TiO_2 and orthorhombic Li_xTiO_2.[9,30,31] The peaks are well defined and only ∼5/10 mV shifts are observed for low doping concentration. Higher concentration (10%) leads to a change in the charge/discharge mechanism already after 50 cycles. Previous studies demonstrated that the conductivity of Nb-doped TiO_2 could be tuned by different doping concentrations, while the intercalation reaction remains unaltered.[19] The galvanostatic curves indicate that the doping does affect not only the conductivity but also the lithium insertion. For all the cases, the initial low Coulombic efficiency is associated with irreversible phenomena like Li trapping and side reactions and electrolyte decomposition at the interface.[32] At 0.1% at. doping, the electrodes show the highest Li insertion capacity for the first cycle with a very broad plateau. We suggest that the improved performance is due to the higher conductivity, leading to an increased charge transfer rate. In addition, the low doping concentration seems to have no measurable effect on the reduction of the available Ti^{4+} sites necessary for the Li insertion reaction. These outcomes are in agreement with the electronic structure analysis and the computational findings.

At 1.0% at. doping concentration, instead, the specific capacity is lower than the one from the pristine material. The sample doped at 10% at. shows even lower capacity and a change in the shape of the potential profile. We believe that the reduction in capacity is due to the substitution of the available Ti^{4+} reduction sites in agreement with the DFT calculations. The higher doping concentration at 10% at. results in a significant contribution of Nb in terms of redox activity and, therefore, in the visible change in shape of the potential curve with less extended plateaus. Finally, it is well known that the crystal particle size has a strong impact on the Li insertion behavior in the anatase lattice.[33] In our materials, the increase in Nb doping concentrations leads to an increase in the particle size, which might negatively affect the kinetics of insertion or intercalation reactions. The rate capabilities of the materials are reported in Figure 9a, with the 0.1% at. Nb-doped TiO_2 performing the best. The 0.1% at. doped electrode delivers ∼120 mAh g^{-1} at 10C and ∼53 mAh g^{-1} at the highest rate of 100C, i.e., only 4 s for a complete charge−discharge cycle. The 0.1% doping improves the conductivity of the material while not affecting the lithium insertion. Already at 1.0%, we can see a reduced specific capacity at a low rate with respect to the undoped material, meaning that the niobium doping level decreases the amount of lithium inserted in the structure. However, the conductivity of the 1.0% material is higher than the conductivity of the undoped. Thus, at higher rates, the insertion process is less kinetically limited. It follows that between 30C and 50C, the 1.0% material catches up with the undoped material and eventually surpasses it. The reduction in capacity for the 10% is too high to reach this "inversion point" with the undoped. The capacity retention at 100C with respect
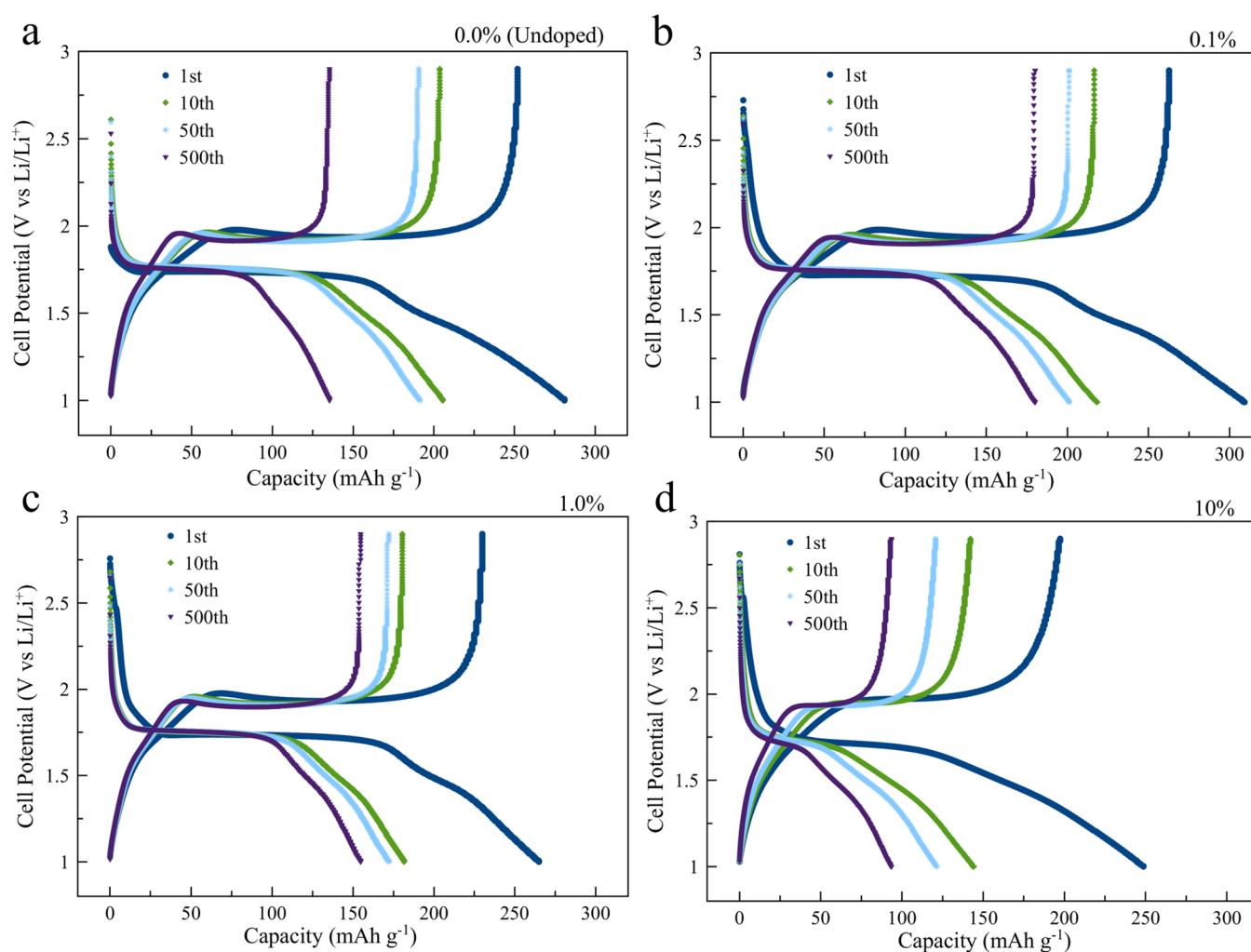
Figure 7. (a) Specific capacity at 1C. (b) Coulombic efficiency of the Nb-doped and undoped TiO_2 electrodes.

capacity at 1C of the Nb-doped electrodes as well as for the undoped TiO_2 (0.0%). After an initial irreversibility, typically observed for TiO_2 materials, the capacity of all the doped materials remains stable over 500 cycles, suggesting a doping-induced mitigation of the capacity fading process normally affecting anatase.[29] Only the 0.1% at. Nb-doped sample shows a higher discharge capacity compared to the undoped TiO_2 and retains 180 mAh g^{-1} at 1C (330 mA g^{-1}, associated to the tetragonal-phase Li_1TiO_2 for all the samples) after 500 cycles.

Figure 8. Galvanostatic charge/discharge curves at 1C: (a) undoped TiO_2, (b) 0.1% at. Nb, (c) 1.0% at. Nb, and (d) 10% at. doping.

to 1C is 26%, compared to the 14% for the undoped electrode and the 28% of the 1% at. Nb doping. It confirms the increase in conductivity due to the doping process and the improvement in charge transfer kinetics in connection to the fast Li-ion diffusion into the mesoporous bead's morphology.

Based on these results, we decided to perform prolonged cycling tests at a high rate for the 0.1 and 1.0% at. Nb-doped samples. Typically, 2C and 5C fast charging processes are considered state of the art.[34,35] In Figure 8b, we report the long-term behavior of the discharge capacity at 10C of the Nb-doped electrodes, revealing an excellent stability for both materials. The 0.1% at. Nb-doped TiO_2 results in better performance both at slow and fast charging, exhibiting ~110 mAh g^{-1} at 10C even after 1000 cycles. Considering the easy synthesis, the cheap materials, and the great performance at a high rate (10C), our results are highly promising and competitive with similar anatase and rutile morphologies reported in literature[36,37] for fast-charging high-rate Li-ion battery applications, as shown in Table 2. More importantly, as the calculations suggested, there is a correlation between the Fermi level of the Nb-doped anatase and the electrochemical performance. Small doping levels enhance the metallic-like character and, with that, the battery performance. These findings point to a general prediction for all n-type (fluorine, tantalum, molybdenum, etc.) doped anatase materials, opening the possibility to tailor the amount of n-type doping necessary for enhancing the electrochemical performance of the anatase-type anodes.

CONCLUSIONS

The present work reports a detailed study on the effect of Nb^{5+} doping in anatase materials for high-rate Li-ion batteries. The pentavalent donor-type doping plays a fundamental role in increasing the electronic conductivity of the materials. The sol−gel synthesis of Nb-doped microbeads allows the formation of phase-pure doped anatase with spherical morphology and high degree of mesoporosity. Computational and experimental data demonstrate that a tailored amount (from 0.1% up to 1.0%) of n-type doping enhances the metallic character without interfering with the redox reaction of Ti^{4+}/Ti^{3+}. We demonstrated the correlation between niobium doping and the Ti^{4+} sites available for lithium intercalation. The electrodes exhibit remarkable stability after prolonged slow (1C) and fast (10C) cycling. The best performing Nb-doped TiO_2 material has a Nb concentration of 0.1% at., which results in high and reversible charge/discharge capacities of 180 mAh g^{-1} at 1C (330 mA g^{-1}) after 500 cycles and 110 mAh g^{-1} at 10C (3300 mA g^{-1}) even after 1000 cycles. The results underline the concrete possibility of using TiO_2 materials for practical applications in fast-charging (up to 10C) Li-ion batteries. We believe that these results are
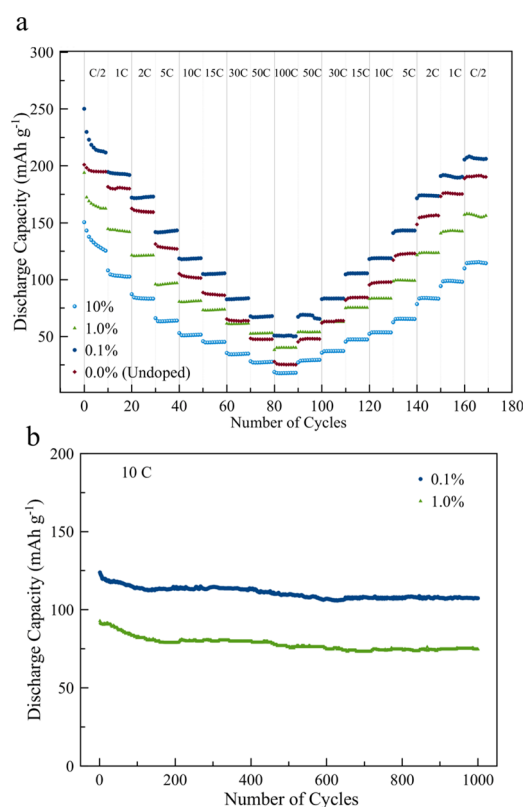
Figure 9. (a) Charge/discharge rate performance of the electrodes from 0.5C to 100C. (b) Capacity retention at 1C of 0.1 and 1% Nb-doped TiO_2 electrodes up to 1000 cycles.

applicable to other types of *n*-type dopants and, in general, for anatase-type materials and that they can be of high interest for battery applications.

■ EXPERIMENTAL SECTION

Material Synthesis Process. Titanium(IV) isopropoxide (TIP) (97 + %), ammonium hydroxide solution (30−33%), potassium chloride (KCl) (99.99%, trace metal basis), 1-hexadecylamine (HDA) (technical, 90%), and niobium(V) ethoxide (99.95%, trace metal basis) were purchased from Sigma Aldrich and used as received. The mesoporous anatase beads doped with Nb^{5+} were prepared according to the procedure proposed by Chen *et al.*[43] and later optimized[44,45] by the controlled hydrolysis of TIP in a hydroalcoholic medium for 18 h with HDA as a structure-directing agent and KCl to regulate ionic strength followed by autoclaving at 160 °C in hydroalcoholic ammonia for 16 h and calcining at 500 °C for 2 h in air of the obtained solid. Niobium was, for the first time with this kind of synthesis, introduced by substituting the appropriate amount of TIP with niobium(V) ethoxide during the synthesis. In detail, 9 mL of TIP (8.592 g, 30 mmol) was used for the pure TiO_2. The necessary amount of atomic doping (7.6 μL for the 0.1%, 76 μL for the 1%, and 760 μL for the 10%) was dispersed by ultrasonication in 1 mL of absolute ethanol and mixed with the appropriate quantity of TIP before the addition to hydroalcoholic HDA−KCl.

Structural and Morphological Characterization. Structural analysis of the produced solids was performed by powder X-ray diffraction (XRD) on a D8-Advance Bruker AXS diffractometer in a scanning range of 10−80° using Cu Kα1 radiation having a wavelength of 0.15406 nm. The angular range covered was 10−90° (2θ), and the angular resolution was 0.001°. A 0.04 rad Soller slit, a 1° divergence slit, and a 20 mm mask were used on the incident beam path, while a 6.6 mm anti-scatter slit and a 0.04 rad collimator were used on the diffracted beam path. The Rietveld analysis of the obtained patterns was performed using the MAUD software package.[46] N2 adsorption and desorption isotherms were recorded at −196 °C using a Micromeritics Tristar instrument. The pore volume and pore size distribution were determined from the adsorption isotherm and the BJH (Barret−Joyner−Halenda) method, and the specific surface area was calculated by the BET (Brunauer−Emmet−Teller) multipoint method. The morphology of the TiO_2 beads was further investigated with a Hitachi SU82200 field emission scanning electron microscope (FE-SEM). EDX analysis was performed with a Hitachi SU82200 field emission scanning electron microscope (FE-SEM). High-resolution transmission electron microscopy experiments (HRTEM) were performed using a JEOL 2100F operating at 200 kV with a point resolution of 1.9 Å. Samples were prepared by crushing powders in ethanol and deposited on a holey carbon-filmed copper grid. Raman spectra were aquired using a Dilor LabRam confocal Raman spectrometer equipped with a Peltier cooled CCD. Spectra were recorded using a 633 nm incident laser, on a 1800 groves/mm grating, three accumulations of 10 s acquisitions, with the samples placed within a capillary tube.

Computational Methods. Density functional theory (DFT) calculations were performed using the projector-augmented wave[47] method as implemented in the VASP[47−49] code. Initially, all structures have been rendered to an energy minimum following a full geometry optimization by means of GGA-PBE[50] as exchange−correlation functional with a plane-wave cutoff energy of 550 eV and integration in reciprocal space considered only at the gamma-point. Thereafter, the electronic structure has been obtained for each compound using the hybrid functional HSE06[25] with a higher plane-wave cutoff energy of 600 eV. All the theoretical analysis has followed this final calculation, e.g., electronic density of states, lithiation voltages, etc. Moreover, spin polarization effects have been considered in all computational steps.

The TiO_2 anatase has been modeled considering a 5 × 5 × 2 supercell with 100 Ti atoms and 200 O atoms. The 1.0% at. Nb-doped sample is immediately obtained by a direct substitution of one Ti by a Nb atom. However, for the 10% at. Nb-doped sample, a more realistic structure can be obtained by using the special quasi-random structure[51] method as implemented in the Quantum ATK Q-2019.12[52] software. In view of the actual computational limitations, the proper modeling of the 0.1% compound lies beyond traditional DFT approaches. It would require a supercell with 1000 Ti atoms to represent this dopant concentration. Therefore, this case is not included in the ab initio modeling. In this approach, an evolutionary algorithm is used to permute the position of the targeted atoms in order to achieve a final configuration closer to the one of an ideal random alloy. As a benchmark, Figure S1 shows the calculated powder XRD of these structures. Additionally, the calculated band gap

Table 2. Comparison at High C Rates (1C and 10C) of Different TiO_2 Materials Reported in Literature[a]

material (TiO_2)	specific capacity at 1C (mAh g^{-1})	specific capacity at 10C (mAh g^{-1})	capacity retention (%)	ref
NPs	170	115	∼83 (100 cycles at 1C)	38
NTs	220	100	∼93 (50 cycles at 1C)	39
porous core/shell particles	165	126	∼86 (100 cycles at 1C)	40
oxygen-deficient blue NPs	178	96	∼100 (10,000 cycles at 50C)	41
Cr/N-codoped MSs	200	127	∼100 (300 cycles at 5C)	42

[a]NPs, nanoparticles; NTs, nanotubes; and MSs, mesoporous microspheres.

of 3.28 eV for the undoped anatase TiO_2 is here provided as complementary information to be correlated with a widely accepted experimental value of 3.2 eV.[53−55] For each compound, one Li atom has been added afterward to obtain the lithiation potential (vs Li/Li$^+$), considering the scenarios where the Li uptake could happen closer or farther from the doping sites on the Nb-doped phases, henceforth denoted as Nb-rich and Nb-poor scenarios, respectively.

The lithiation voltage has been calculated by following the equation in accordance with previous works in the literature:[56,57]

$$V(x) = -\frac{E(\text{Li}_{x_1}\mathcal{H}) - E(\text{Li}_{x_0}\mathcal{H}) - (x_1 - x_0)E(\text{Li})}{x_1 - x_0} \qquad (3)$$

where H is the electrode material being lithiated and x_0 and x_1 are the amounts of initial and added Li, respectively.

Electrode Preparation. The electrodes were prepared by mixing the mesoporous anatase undoped and doped beads with Super P (Alfa Aesar) and Kynar PVDF binder (Arkema) in NMP (N-methyl-2-pyrrolidone, anhydrous, 99.5%, Sigma Aldrich) and finally depositing the mixture on a copper current collector. First, mesoporous anatase beads were mixed by ball milling at 10 Hz for 10 min in a ZrO_2-coated cup with ZrO_2 balls in a Retsch MM400 ball mill. The ball-milled mixture was transferred to a glass vial, and Super-P and Kynar 5% (w/w) solution in NMP were added. The solution was stirred overnight in a capped vial, forming a slurry having a weight ratio of TiO_2/Super-P/PVDF of 8:1:1. The slurry was coated onto a copper foil through a TQC AB3400 motorized automatic film applicator. A stainless-steel doctor blade (Wellcos Co.) was used to obtain a 150 μm-thick coating of the slurry. The electrode sheets were dried for 1 day under ambient conditions in a fume hood followed by drying in a vacuum oven at 80 °C and 20 mbar for 2 h.

Electrochemical Analysis and Device Testing. The electrochemical response of the electrodes as anodes was tested in Li-ion half cells. The electrodes (∼10 mm diameter, 1.5 mg cm^{-2} active material) were transferred to a glovebox (H_2O and O_2 less than 1 ppm) and dried under vacuum at 80 °C in a Buchi oven. Coin cells were assembled in an argon-filled glovebox using CR2032 housings. Glass microfiber (Sigma Aldrich) was used as the separator, soaked with 30 μL of commercial electrolyte LP30 solution (Sigma Aldrich), while a lithium metal disk was used as an anode (diameter, 11 mm; areal density, 4 mg cm^{-2}). Galvanostatic charge−discharge tests were performed between 1 and 2.9 V using a Scribner 580 battery cycler. EIS spectra were recorded with a Bio-Logic VMP-3 potentiostat between 1 MHz and 100 mHz.

■ ASSOCIATED CONTENT

(SI) Supporting Information

The Supporting Information is available free of charge at https://pubs.acs.org/doi/10.1021/acsaem.0c02157.

Photographs of Nb-doped TiO_2 powders doped at 1.0% at. and 10% at. Nb; XRD of the pure TiO_2; calculated powder XRD of the anatase TiO_2 and 1.0% at. and 10% at. Nb-doped TiO_2 (Vesta); SEM images of the pure, 1.0%, and 10% samples (high-resolution Png images); EDX spectra and relative quantitative analysis (high-resolution Png image); N2 adsorption curves for all the samples (high-resolution Png); lithiated structures of 1.0% at. and 10% at. Nb-doped TiO_2 (Vesta); and differential curves for all the samples (high-resolution Png) (PDF)

■ AUTHOR INFORMATION

Corresponding Authors

Carmen Cavallo − *Centre for Materials Science and Nanotechnology, Department of Chemistry, Oslo University, 0371 Oslo, Norway; Department of Physics, Chalmers University of Technology, 412 96 Gothenburg, Sweden;* orcid.org/0000-0003-1931-3018; Email: carmen.cavallo@smn.uio.no

Aleksandar Matic − *Department of Physics, Chalmers University of Technology, 412 96 Gothenburg, Sweden;* orcid.org/0000-0003-1795-7805; Email: matic@chalmers.se

Authors

Giulio Calcagno − *Department of Chemistry and Chemical Engineering, Chalmers University of Technology, 412 96 Gothenburg, Sweden*

Rodrigo Pereira de Carvalho − *Materials Theory Division, Department of Physics and Astronomy, Ångström Laboratory, Uppsala University, 751 20 Uppsala, Sweden*

Matthew Sadd − *Department of Physics, Chalmers University of Technology, 412 96 Gothenburg, Sweden*

Bruno Gonano − *Centre for Materials Science and Nanotechnology, Department of Chemistry, Oslo University, 0371 Oslo, Norway*

C. Moyses Araujo − *Materials Theory Division, Department of Physics and Astronomy, Ångström Laboratory, Uppsala University, 751 20 Uppsala, Sweden;* orcid.org/0000-0001-5192-0016

Anders E.C. Palmqvist − *Department of Chemistry and Chemical Engineering, Chalmers University of Technology, 412 96 Gothenburg, Sweden;* orcid.org/0000-0002-7579-3936

Complete contact information is available at:
https://pubs.acs.org/10.1021/acsaem.0c02157

Author Contributions

C.C. and G.C. synthesized and characterized the materials and performed all the electrochemical characterization of the devices. R.P.C. and C.M.A. led the computational part and performed calculations. M.S. performed the Raman spectroscopy and analyzed the data. B.G. captured the TEM images and analyzed the data. C.C., G.C., and R.P.C. wrote the manuscript. C.C., A.P., and A.M. led the project. All the authors contributed to discussion and editing of the manuscript draft.

Notes

The authors declare no competing financial interest.

■ ACKNOWLEDGMENTS

■ REFERENCES

(1) Madian, M.; Eychmüller, A.; Giebeler, L. Current Advances in TiO_2-Based Nanostructure Electrodes for High Performance Lithium Ion Batteries. *Batteries* **2018**, *4*, 7.

(2) Lu, J.; Chen, Z.; Pan, F.; Cui, Y.; Amine, K. High-Performance Anode Materials for Rechargeable Lithium-Ion Batteries. *Electrochem. Energy Rev.* **2018**, *1*, 35−53.

(3) Ball, S.; Clark, J.; Cookson, J. Battery Materials Technology Trends and Market Drivers for Automotive Applications. *Johnson Matthey Technol. Rev.* **2020**, *64*, 287−297.

(4) Jaffe, S. Vulnerable Links in the Lithium-Ion Battery Supply Chain. *Joule* **2017**, *1*, 225−228.

(5) Finegan, D. P.; Quinn, A.; Wragg, D. S.; Colclasure, A. M.; Lu, X.; Tan, C.; Heenan, T. M. M.; Jervis, R.; Brett, D. J. L.; Das, S.; Gao, T.; Cogswell, D. A.; Bazant, M. Z.; Di Michiel, M.; Checchia, S.; Shearing, P. R.; Smith, K. Spatial Dynamics of Lithiation and Lithium Plating during High-Rate Operation of Graphite Electrodes. *Energy Environ. Sci.* **2020**, *13*, 2570−2584.

(6) Lu, L.; Han, X.; Li, J.; Hua, J.; Ouyang, M. A Review on the Key Issues for Lithium-Ion Battery Management in Electric Vehicles. *J. Power Sources* **2013**, *226*, 272−288.

(7) Li, H.; Wang, Z.; Chen, L.; Huang, X. Research on Advanced Materials for Li-Ion Batteries. *Adv. Mater.* **2009**, 4593−4607.

(8) Liu, Y.; Yang, Y. Recent Progress of TiO$_2$-based Anodes for Li Ion Batteries. *J. Nanomater.* **2016**, *2016*, 1−15.

(9) Calcagno, G.; Lotsari, A.; Dang, A.; Lindberg, S.; Palmqvist, A. E. C.; Matic, A.; Cavallo, C. Fast Charging Negative Electrodes Based on Anatase Titanium Dioxide Beads for Highly Stable Li-Ion Capacitors. *Mater. Today Energy* **2020**, *16*, 100424.

(10) Koketsu, T.; Ma, J.; Morgan, B. J.; Body, M.; Legein, C.; Goddard, P.; Borkiewicz, O. J.; Strasser, P.; Dambournet, D. Exploiting Cationic Vacancies for Increased Energy Densities in Dual-Ion Batteries. *Energy Storage Mater.* **2020**, *25*, 154−163.

(11) Gardecka, A. J.; Lübke, M.; Armer, C. F.; Ning, D.; Reddy, M. V.; Williams, A. S.; Lowe, A.; Liu, Z.; Parkin, I. P.; Darr, J. A. Nb-Doped Rutile Titanium Dioxide Nanorods for Lithium-Ion Batteries. *Solid State Sci.* **2018**, *83*, 115−121.

(12) Raghav, A.; Hanindriyo, A. T.; Utimula, K.; Abbasnejad, M.; Maezono, R.; Panda, E. Electronic Structure and Defect States of Undoped and (Nb, Ta)-Doped Anatase Using Density Functional Theory. *Mater. Sci.* **2020**, 1−36. arXiv:2002.05351

(13) Matsubara, M.; Saniz, R.; Partoens, B.; Lamoen, D. Doping Anatase TiO$_2$ with Group V-b and VI-b Transition Metal Atoms: A Hybrid Functional First-Principles Study. *Phys. Chem. Chem. Phys.* **2017**, *19*, 1945−1952.

(14) Lübke, M.; Shin, J.; Marchand, P.; Brett, D.; Shearing, P.; Liu, Z.; Darr, J. A. Highly Pseudocapacitive Nb-Doped TiO$_2$ High Power Anodes for Lithium-Ion Batteries. *J. Mater. Chem. A* **2015**, *3*, 22908−22914.

(15) Fehse, M.; Cavaliere, S.; Lippens, P. E.; Savych, I.; Iadecola, A.; Monconduit, L.; Jones, D. J.; Rozière, J.; Fischer, F.; Tessier, C.; Stievano, L. Nb-Doped TiO$_2$ Nanofibers for Lithium Ion Batteries. *J. Phys. Chem. C* **2013**, *117*, 13827−13835.

(16) Körner, W.; Elsässer, C. Density Functional Theory Study of Dopants in Polycrystalline TiO$_2$. *Phys. Rev. B* **2011**, *83*, 205315.

(17) Sheppard, L. R.; Bak, T.; Nowotny, J. Electrical Properties of Niobium-Doped Titanium Dioxide. 1. Defect Disorder. *J. Phys. Chem. B* **2006**, *110*, 22447−22454.

(18) Yang, K.; Dai, Y.; Huang, B.; Feng, Y. P. First-Principles GGA +UStudy of the Different Conducting Properties in Pentavalent-Ion-Doped Anatase and Rutile TiO$_2$. *J. Phys. D: Appl. Phys.* **2014**, *47*, 275101 (1-9).

(19) Yue, J.; Suchomski, C.; Voepel, P.; Ellinghaus, R.; Rohnke, M.; Leichtweiss, T.; Elm, M. T.; Smarsly, B. M. Mesoporous Niobium-Doped Titanium Dioxide Films from the Assembly of Crystalline Nanoparticles: Study on the Relationship between the Band Structure, Conductivity and Charge Storage Mechanism. *J. Mater. Chem. A* **2017**, *5*, 1978−1988.

(20) Lindberg, S.; Cavallo, C.; Calcagno, G.; Navarro-Suárez, A. M.; Johansson, P.; Matic, A. Electrochemical Behaviour of Nb-Doped Anatase TiO$_2$Microbeads in an Ionic Liquid Electrolyte. *Batteries Supercaps* **2020**, *3*, 1233.

(21) Tomaszewska, A.; Chu, Z.; Feng, X.; O'Kane, S.; Liu, X.; Chen, J.; Ji, C.; Endler, E.; Li, R.; Liu, L.; Li, Y.; Zheng, S.; Vetterlein, S.; Gao, M.; Du, J.; Parkes, M.; Ouyang, M.; Marinescu, M.; Offer, G.; Wu, B. Lithium-Ion Battery Fast Charging: A Review. *eTransportation* **2019**, *1*, 100011.

(22) Logan, E. R.; Dahn, J. R. Electrolyte Design for Fast-Charging Li-Ion Batteries. *Trends Chem.* **2020**, *2*, 354−366.

(23) Kong, L.; Wang, C.; Zheng, H.; Zhang, X.; Liu, Y. Defect-Induced Yellow Color in Nb-Doped TiO$_2$ and Its Impact on Visible-Light Photocatalysis. *J. Phys. Chem. C* **2015**, *119*, 16623−16632.

(24) International Center for Diffraction Data, Data Base JCPDS CARD = 78-2486.

(25) Heyd, J.; Scuseria, G. E.; Ernzerhof, M. Hybrid Functionals Based on a Screened Coulomb Potential. *J. Chem. Phys.* **2003**, *118*, 8207−8215.

(26) Lee, D. Y.; Park, J. H.; Kim, Y. H.; Lee, M. H.; Cho, N. I. Effect of Nb Doping on Morphology, Crystal Structure, Optical Band Gap Energy of TiO2 Thin Films. *Curr. Appl. Phys.* **2014**, *14*, 421−427.

(27) Latini, A.; Cavallo, C.; Aldibaja, F. K.; Gozzi, D.; Carta, D.; Corrias, A.; Lazzarini, L.; Salviati, G. Efficiency Improvement of DSSC Photoanode by Scandium Doping of Mesoporous Titania Beads. *J. Phys. Chem. C* **2013**, *117*, 25276−25289.

(28) Fleischmann, S.; Mitchell, J. B.; Wang, R.; Zhan, C.; Jiang, D. E.; Presser, V.; Augustyn, V. Pseudocapacitance: From Fundamental Understanding to High Power Energy Storage Materials. *Chem. Rev.* **2020**, *120*, 6738−6782.

(29) Zhang, W.; Luo, N.; Huang, S.; Wu, N. L.; Wei, M. Sulfur-Doped Anatase TiO$_2$ as an Anode for High-Performance Sodium-Ion Batteries. *ACS Appl. Energy Mater.* **2019**, *2*, 3791−3797.

(30) Yang, J.; Wang, Y.; Li, W.; Wang, L.; Fan, Y.; Jiang, W.; Luo, W.; Wang, Y.; Kong, B.; Selomulya, C.; Liu, H. K.; Dou, S. X.; Zhao, D. Amorphous TiO$_2$Shells: A Vital Elastic Buffering Layer on Silicon Nanoparticles for High-Performance and Safe Lithium Storage. *Adv. Mater.* **2017**, *29*, 1700523. . 2017, 9 (3), pp

(31) Luo, W.; Wang, Y.; Wang, L.; Jiang, W.; Chou, S. L.; Dou, S. X.; Liu, H. K.; Yang, J. Silicon/Mesoporous Carbon/Crystalline TiO$_2$ Nanoparticles for Highly Stable Lithium Storage. *ACS Nano* **2016**, *10*, 10524−10532.

(32) Ventosa, E.; Madej, E.; Zampardi, G.; Mei, B.; Weide, P.; Antoni, H.; La Mantia, F.; Muhler, M.; Schuhmann, W. Solid Electrolyte Interphase (SEI) at TiO$_2$ Electrodes in Li-Ion Batteries: Defining Apparent and Effective SEI Based on Evidence from X-Ray Photoemission Spectroscopy and Scanning Electrochemical Micros-copy. *ACS Appl. Mater. Interfaces* **2017**, *9*, 3123−3130.

(33) Wagemaker, M.; Borghols, W. J. H.; Mulder, F. M. Large Impact of Particle Size on Insertion Reactions. A Case for Anatase LixTiO2. *J. Am. Chem. Soc.* **2007**, *129*, 4323−4327.

(34) Zhang, Y.; Liu, X.; Wu, L.; Dong, W.; Xia, F.; Chen, L.; Zhou, N.; Xia, L.; Hu, Z. Y.; Liu, J.; Mohamed, H. S. H.; Li, Y.; Zhao, Y.; Chen, L.; Su, B. L. A Flexible, Hierarchically Porous PANI/MnO$_2$ Network with Fast Channels and an Extraordinary Chemical Process for Stable Fast-Charging Lithium-Sulfur Batteries. *J. Mater. Chem. A* **2020**, *8*, 2741−2751.

(35) De Souza, J. P.; Lee, Y. S.; Sadana, D. K. Thin-Film Lithium-Ion Battery with Fast Charging Speed. U.S. Patent No. 10,553,898. 4 Feb. 2020.

(36) Usui, H.; Yoshioka, S.; Wasada, K.; Shimizu, M.; Sakaguchi, H. Nb-Doped Rutile TiO2: A Potential Anode Material for Na-Ion Battery. *ACS Appl. Mater. Interfaces* **2015**, *7*, 6567−6573.

(37) Tanaka, Y.; Usui, H.; Domi, Y.; Ohtani, M.; Kobiro, K.; Sakaguchi, H. Mesoporous Spherical Aggregates Consisted of Nb-Doped Anatase TiO$_2$ Nanoparticles for Li and Na Storage Materials. *ACS Appl. Energy Mater.* **2018**, *2*, 636−643.

(38) Kubiak, P.; Fröschl, T.; Hüsing, N.; Hörmann, U.; Kaiser, U.; Schiller, R.; Weiss, C. K.; Landfester, K.; Wohlfahrt−Mehrens, M. TiO2 Anatase Nanoparticle Networks: Synthesis, Structure, and Electrochemical Performance. *Small* **2011**, 1690.

(39) Gentili, V.; Brutti, S.; Hardwick, L. J.; Armstrong, A. R.; Panero, S.; Bruce, P. G. Lithium Insertion into Anatase Nanotubes. *Chem. Mater.* **2012**, *24*, 4468−4476.

(40) Cai, Y.; Wang, H. E.; Zhao, X.; Huang, F.; Wang, C.; Deng, Z.; Li, Y.; Cao, G.; Su, B. L. Walnut-like Porous Core/Shell TiO_2 with Hybridized Phases Enabling Fast and Stable Lithium Storage. *ACS Appl. Mater. Interfaces* **2017**, *9*, 10652−10663.

(41) Hao, Z.; Chen, Q.; Dai, W.; Ren, Y.; Zhou, Y.; Yang, J.; Xie, S.; Shen, Y.; Wu, J.; Chen, W.; Xu, G. Q. Oxygen-Deficient Blue TiO_2 for Ultrastable and Fast Lithium Storage. *Adv. Energy Mater.* **2020**, *10*, 1903107.

(42) Bi, Z.; Paranthaman, M. P.; Guo, B.; Unocic, R. R.; Meyer, H. M., III; Bridges, C. A.; Sun, X. G.; Dai, S. High Performance Cr, N-Codoped Mesoporous TiO_2 Microspheres for Lithium-Ion Batteries. *J. Mater. Chem. A* **2014**, *2*, 1818−1824.

(43) Chen, D.; Cao, L.; Huang, F.; Imperial, P.; Cheng, Y.-B.; Caruso, R. A. Synthesis of Monodisperse Mesoporous Titania Beads with Controllable Diameter, High Surface Areas, and Variable Pore Diameters (14-23 Nm). *J. Am. Chem. Soc.* **2010**, *132*, 4438−4444.

(44) Cavallo, C.; Salleo, A.; Gozzi, D.; Di Pascasio, F.; Quaranta, S.; Panetta, R.; Latini, A. Solid Solutions of Rare Earth Cations in Mesoporous Anatase Beads and Their Performances in Dye-Sensitized Solar Cells. *Sci. Rep.* **2015**, *5*, 1−15.

(45) Cavallo, C.; Mantella, V.; Dulong, A.; Di Pascasio, F.; Quaranta, S. Investigation on Zr-, Hf-, and Ta-Doped Submicrometric Beads for DSSC Photoanodes. *Appl. Phys. A* **2017**, *123*, 180.

(46) Lutterotti, L.; Matthies, S.; Wenk, H. R. *Proceedings of the 12th International Conference on Textures of Materials (ICOTOM '99)*; ICOTOM 1 (1999) 1599−1604.

(47) Kresse, G.; Joubert, D. From Ultrasoft Pseudopotentials to the Projector Augmented-Wave Method. *Phys. Rev. B* **1999**, *59*, 1758−1775.

(48) Kresse, G.; Hafner, J. Ab Initio Molecular Dynamics for Liquid Metals. *Phys. Rev. B* **1993**, *47*, 558−561.

(49) Kresse, G.; Furthmüller, J. Efficient Iterative Schemes for Ab Initio Total-Energy Calculations Using a Plane-Wave Basis Set. *Phys. Rev. B* **1996**, *54*, 11169−11186.

(50) Perdew, J. P.; Burke, K.; Ernzerhof, M. Generalized Gradient Approximation Made Simple. *Phys. Rev. Lett.* **1996**, *77*, 3865−3868.

(51) Van De Walle, A.; Tiwary, P.; De Jong, M.; Olmsted, D. L.; Asta, M.; Dick, A.; Shin, D.; Wang, Y.; Chen, L. Q.; Liu, Z. K. Efficient Stochastic Generation of Special Quasirandom Structures. *Calphad* **2013**, *42*, 13−18.

(52) Smidstrup, S.; Markussen, T.; Vancraeyveld, P.; Wellendorff, J.; Schneider, J.; Gunst, T.; Verstichel, B.; Stradi, D.; Khomyakov, P. A.; Vej-Hansen, U. G.; Lee, M.-E.; Chill, S. T.; Rasmussen, F.; Penazzi, G.; Corsetti, F.; Ojanperä, A.; Jensen, K.; Palsgaard, M. L. N.; Martinez, U.; Blom, A.; Brandbyge, M.; Stokbro, K. QuantumATK: An Integrated Platform of Electronic and Atomic-Scale Modelling Tools. *J. Phys. Condens. Matter* **2020**, *32*, No. 015901.

(53) Garzon-Roman, A.; Zuñiga-Islas, C.; Quiroga-González, E. Immobilization of Doped TiO_2 Nanostructures with Cu or In inside of Macroporous Silicon Using the Solvothermal Method: Morphological, Structural, Optical and Functional Properties. *Ceram. Int.* **2020**, *46*, 1137−1147.

(54) Triana, C. A.; Araujo, C. M.; Ahuja, R.; Niklasson, G. A.; Edvinsson, T. Electronic Transitions Induced by Short-Range Structural Order in Amorphous TiO_2. *Phys. Rev. B* **2016**, *94*, 165129.

(55) Dou, M.; Persson, C. Comparative Study of Rutile and Anatase SnO_2 and TiO_2: Band-Edge Structures, Dielectric Functions, and Polaron Effects. *J. Appl. Phys.* **2013**, *113*, No. 083703.

(56) Carvalho, R. P.; Marchiori, C. F. N.; Brandell, D.; Araujo, C. M. Tuning the Electrochemical Properties of Organic Battery Cathode Materials: Insights from Evolutionary Algorithm DFT Calculations. *ChemSusChem* **2020**, *13*, 2402−2409.

(57) Marchiori, C. F. N.; Brandell, D.; Araujo, C. M. Predicting Structure and Electrochemistry of Dilithium Thiophene-2,5-Dicarboxylate Electrodes by Density Functional Theory and Evolutionary Algorithms. *J. Phys. Chem. C* **2019**, *123*, 4691−4700.